Article

Conversion of Interfacial Chemical Bonds for Inducing Efficient Photoelectrocatalytic Water Splitting

Xi Chen, Xuchen Zheng, Lu Qi, Yurui Xue,* and Yuliang Li*

Read Online

ACCESS | Metrics & More | Article Recommendations | SI Supporting Information

ABSTRACT: Sp-C-hybridized alkyne bonds present the natural advantages of interacting with metal atoms and have the ability to generate a large number of new catalytic active sites on the surface and the interfaces, thus greatly promoting the efficient progress of various light/electrochemical reactions. In this work, we have successfully fabricated a novel type of interfacial structure containing sp-C−Mo/O bonds and mixed Mo valence states with outstanding catalytic activity and stability for photoelectrocatalytic (PEC) overall water splitting in a wide pH range (0−14), due to the presence of sp-carbon-rich graphdiyne. For example, in alkaline conditions (pH = 14), the overpotentials of oxygen and hydrogen evolution reactions at 10 mA cm^{-2} are 165 and 8 mV. When being used as an electrolyzer, the cell voltage of this catalyst is only 1.40 V to achieve 10 mA cm^{-2}. The high PEC activity of graphdiyne@molybdenum oxide originates from the conversion of chemical bonds at the sp-C hybrid interface and the coexistence of multivalent states of molybdenum, triggering a large number of catalytic active sites, greatly promoting charge transfer and lowering water dissociation energy.

KEYWORDS: *interfacial chemical bonds, photoelectrocatalytic water splitting, hydrogen generation*
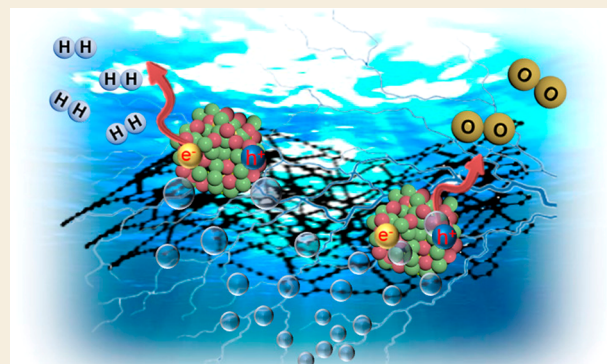
1. INTRODUCTION

Photoelectrocatalytic (PEC) water splitting is a model of solar energy utilization to directly dissociate water (H_2O) into green hydrogen (H_2) at ambient temperatures and low overpotentials, with no greenhouse gas emissions.[1−6] Considerable efforts have recently been devoted to design and synthesize new catalysts with highly catalytic performances. As an intrinsic wide bandgap n-type semiconductor (bandgap ≈ 3.2 eV), molybdenum oxide (MoO_3), with the potential as an excellent catalyst, has been extensively studied for photocatalytic applications in recent years.[7] However, obtaining molybdenum-oxide-based materials with the efficient capture and conversion of solar energy into hydrogen fuel becomes highly challenging, due to its low intrinsic conductivity and low light response.

In view of the above issues, improving the conductivity and light capture abilities of molybdenum-oxide-based materials is the core problem. Therefore, designing a reasonable catalyst interface structure for accelerating the interface electron transfer and promoting the charge polarization on the interfaces is considered to be a very effective strategy.[8−10] Such an interface structure plays critical roles in improving the abilities of the conductivity and light capture and then leads to the catalytic activity and selectivity in various reactions.[11−17] The combinations of metal catalysts and carbon materials are outstanding examples to form heterostructured interfaces with optimal structures, exposing a large number of active sites and enhancing charge transfer ability.[18,19]

There was no progress in the precise control for synthesis of carbon materials with sp-C-containing active sites. This is due to the limitations of the defect in traditional synthetic chemical methods. Graphdiyne (GDY) is rich in sp-C-hybridized alkyne bonds, which is a rising star on the horizon of carbon materials with many unique properties such as uneven surface charge distribution, high hole mobility, a highly π-conjugated structure, abundant natural pores, and a tunable band gap, and so on.[20−27] These features have established a solid position of GDY in the fields of catalysis, energy conversion and storage, intelligent response, and so on.[28−50] GDY has been demonstrated to be an indispensable material as an excellent hole transfer layer for photocatalysis that effectively prevents the recombination of photogenerated electrons and holes, thus endowing the formed GDY/semiconductor heterostructure with excellent photocatalytic performance.[51−54] As carbon material, GDY is the only all-carbon material that can be grown
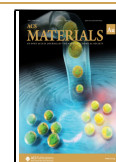
on the surface of arbitrary materials.[20−23,38,55,56] Thus, the ideal interface for multiple-combination selectivity results in improved charge transfer behavior and increased active site numbers, which is very suitable for the construction of high-performance catalysts.

Part of the obvious structural features of GDY, the sp-C-hybridized carbon atoms in alkyne bonds have the natural advantages to interact with metal atoms[57−59] and nonmetal atoms,[36,60] generating newly uniform and highly dispersed active sites of alkyne−"M" and alkyne−"NM" at the interfaces, respectively, which have been demonstrated to significantly improve the interfacial charge transfer behavior and thus enhance catalytic performances. Another outstanding property for GDY is it can efficiently and controllably regulate the valence states of the catalytically active metal atoms to enhance their catalytic activity. Many recent studies from different viewpoints have greatly promoted the rapid development of GDY in the catalytic field.[21−27] However, Mo mainly exists in its high valence state in nature, and the rational and controllable modulation of the forms and types of interfacial chemical bonds and valence states of Mo in molybdenum oxide to generate new intrinsic active sites has never been explored.

With that in mind, we report the construction of a novel structure on the interface between the MoO_x and GDY. The valence states of Mo atoms were found to form new catalytically active sites with accelerated charge transfer and a lowered energy barrier of water dissociation for the enhancement of PEC performances. The self-supported molybdenum oxide quantum dots were synthesized with a size of ∼3.3 nm by GDY as a support (GDY@MoO_x). The sample was characterized and calculated by combination of the use of SEM, HRTEM, HAADF, XPS, and density functional theory calculations. Interestingly, a high active interface was produced by combined C−Mo and C−O bonds and mixed valence states of Mo (5+/6+). The catalytic activity and stability for the PEC hydrogen evolution reaction (HER) and oxygen evolution reaction (OER) as well as overall water splitting (OWS) were greatly enhanced in a wide pH range (0−14).

2. EXPERIMENTAL SECTION

2.1. Materials

Sodium molybdate was purchased from Sigma-Aldrich. Hexabromo-benzene was brought from J&K Scientific. Tetrabutylammonium fluoride and anhydrous zinc chloride were purchased from Alfa Aesar. Tetratriphenylphosphine palladium and N-butyl lithium were brought from Energy Chemistry. Trimethylsilylacetylene was purchased from Shanghai Shaoyuan Reagent Co., Ltd. A Millipore system (RephiLe Bioscience, Ltd., China) was used to purify water. Toluene and tetrahydrofuran were fully refluxed with sodium blocks to remove water. All other reagents were supplied by Tianjin Concord Technology Co., Ltd. and directly used without further purification.

2.2. Preparation of 3D GDY Electrodes

3D GDY electrodes were prepared according to previous literature with a minor modification.[20] In brief, two pieces of carbon fiber cloths (CF, 2 × 3 cm) were added to a 50 mL Teflon-lined stainless-steel autoclave containing 40 mL of pyridine of hexakis[(trimethylsilyl)-ethynyl]benzene (HEB, 0.625 mg mL^{-1}). Then, the reaction system was kept at 110 °C for 12 h. After the completion of the reaction, the obtained two pieces of GDY electrodes were washed thoroughly by acetone and N,N-dimethylformamide, 1 M HCl, deionized water, and acetone to remove residual copper species.

2.3. Preparation of GDY@MoO_x Electrodes

GDY@MoO_x electrodes were synthesized through an in situ reduction method. Briefly, a piece of 1 × 2 cm as-synthesized GDY was immersed into 10 mL of aqueous solution of sodium molybdate (0.3 mg mL^{-1}) for 1 h. Then, the mixture was transferred into a 25 mL Teflon-lined stainless-steel autoclave and held at 120 °C for 8 h. After cooling down to room temperature, the obtained GDY@MoO_x electrode was washed with deionized water several times, followed by being used for photoelectrochemical measurements. For comparison, the control catalyst was synthesized under the same conditions except that the substrate was pure CF, not GDY.

3. RESULTS AND DISCUSSION

3.1. Synthesis and Structural Characterizations

Scheme 1 presents the typical procedure for the synthesis of GDY@MoO_x. Briefly, the GDY@MoO_x was synthesized

Scheme 1. (a) Synthesis Routes and (b) PEC Water Splitting Process for GDY@MoO_x
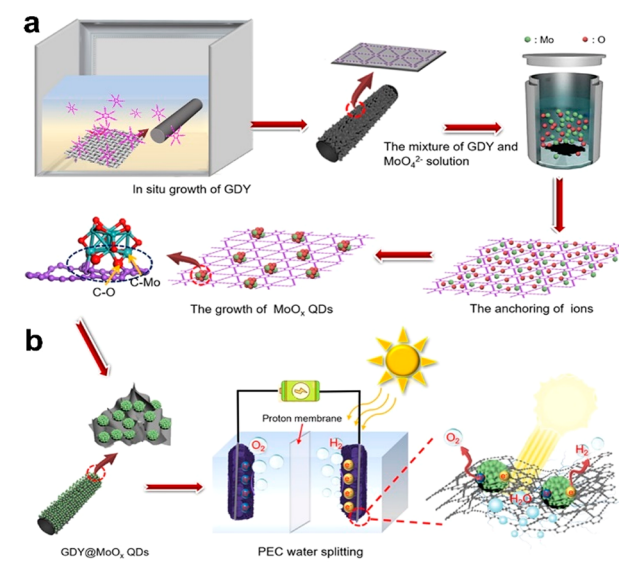
through a two-step strategy including the first fabrication of self-supported GDY nanosheet electrodes by in situ growing GDY films on the surface of the 3D flexible CF network, and the following controllable synthesis of MoO_x on GDY was accompanied by the conversion of "C−O" and "C−Mo" chemical bonds at the sp-C hybrid interface. During the synthesis process, the hydrophobic surface of CF (contact angle = 124°) changed to superhydrophilic for GDY@MoO_x with a complete wetting characteristic (Figure 1a), which profits the transportation of reactants and charges at the electrolyte−catalyst interface. And the color varied from light gray for the CF substrate to black for GDY and GDY@MoO_x electrodes. The as-prepared GDY@MoO_x electrodes also exhibit high flexibility that can be bent and twisted in any direction. These properties make the GDY@MoO_x very suitable for use as an electrode.

Scanning electron microscopy (SEM) images of GDY electrodes show the vertical and uniform growth of a film of two-dimensional GDY nanosheets on CF (Figures 1b,c and S1). This forms a 3D flexible electrode with a porous structure, which benefits the ion/mass diffusion as well as gas evolution and increases the number of active sites. Figure 1d,e shows that the morphology of GDY was well-maintained after the
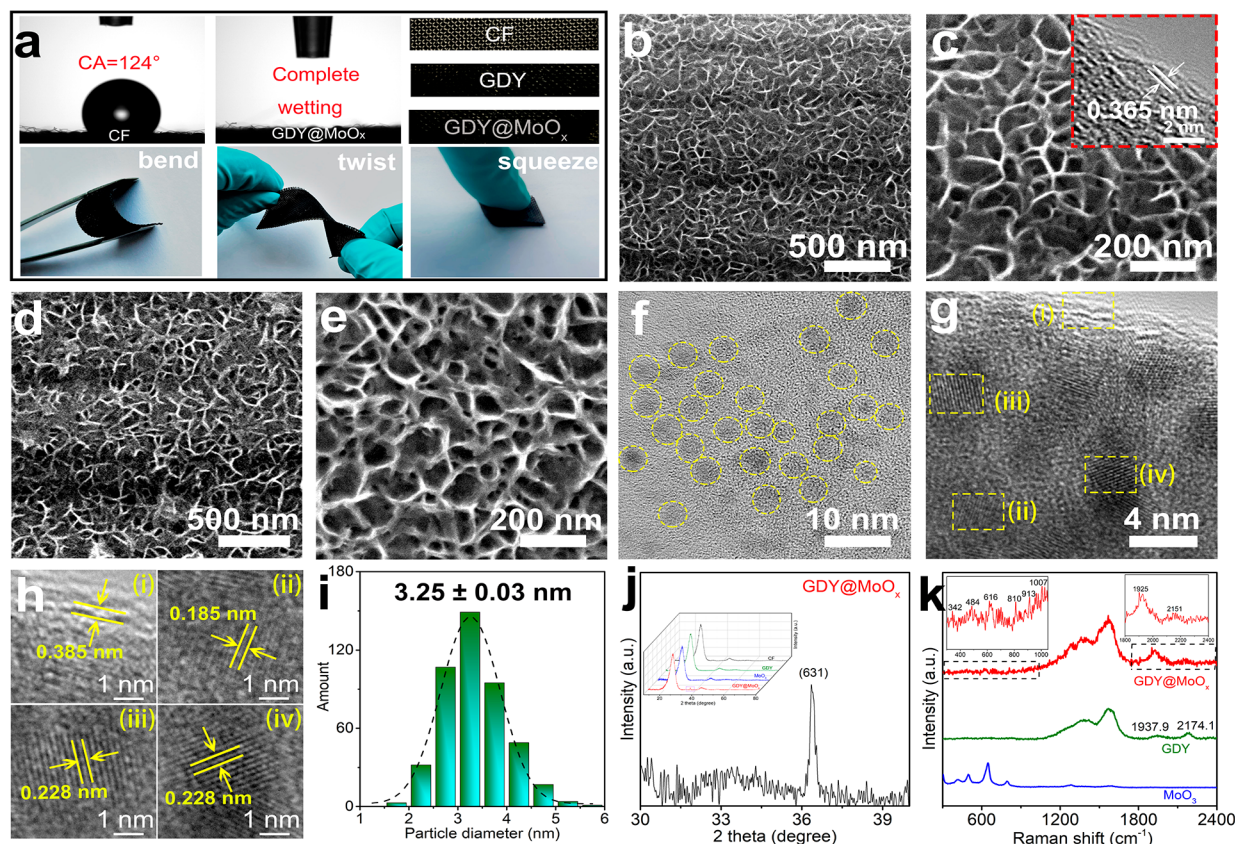
Figure 1. (a) Contact angle measurements of CF and GDY@MoO$_x$. Photographs of CF, GDY, and GDY@MoO$_x$ and different bending configurations for GDY@MoO$_x$. (b,c) SEM images of GDY electrodes (inset: HRTEM image of GDY). (d,e) SEM images and (f–h) HRTEM images of GDY@MoO$_x$. (i) Size distribution of MoO$_x$ QDs on GDY. (j) XRD pattern of GDY@MoO$_x$ (inset: comparative XRD patterns of GDY@MoO$_x$, MoO$_3$, GDY, and CF). (k) Raman spectroscopy of GDY@MoO$_x$, MoO$_3$, and GDY.

anchoring of MoO$_x$ on the surface of GDY, indicating the high structural stability of the catalyst. High-resolution transmission electron microscopy (TEM) images show that the MoO$_x$ QDs were separately and uniformly anchored on the surface of GDY with an average diameter of 3.25 ± 0.03 nm (Figures 1f,i and S2). In contrast, there were only aggregated particles formed on the pure CF surface (Figure S3). This demonstrates the important role of GDY in guiding the controllable synthesis of QDs. HRTEM images show that GDY in GDY@MoO$_x$ possesses a larger spacing distance of 0.385 nm (Figure 1g,h) than GDY (0.365 nm, Figure 1c), which might be due to the interactions between MoO$_x$ QDs and GDY. Without the presence of GDY, the obtained molybdenum oxide exhibits a lattice spacing of 0.202 nm corresponding to MoO$_3$ (Figure S3). Interestingly, MoO$_x$ anchored on GDY shows two types of lattice spacings of the (020) plane of monoclinic α-MoO$_3$ (ICDD PDF # 04−015−7146) and the (631) plane of orthorhombic Mo$_{17}$O$_{47}$ (ICDD PDF # 01−071−0566). This suggests the partial conversion of monoclinic α-MoO$_3$ into the orthorhombic type induced by GDY. The X-ray diffraction (XRD) patterns of the GDY@MoO$_x$ show three peaks at 25, 43, and 36.4° (Figures 1j and S4), which could be assigned to the planes of carbon and the (631) plane of MoO$_x$, respectively. Raman spectra were next measured and shown in Figure 1k. Compared with pristine GDY and MoO$_3$, the peaks for GDY@MoO$_x$ were located at two distinct areas corresponding to the MoO$_x$ QDs[61] and GDY species. This confirms the successful incorporation of GDY with MoO$_x$.[42] The peaks of GDY in GDY@MoO$_x$ exhibit a shift from 1937.9

and 2174.1 cm^{-1} (GDY) to 1925.0 and 2151.0 cm^{-1} (GDY@MoO$_x$), which further confirms the interactions between MoO$_x$ and GDY (Figures S4 and S5).

The X-ray photoelectron spectroscopy (XPS), electron energy loss spectroscopy (EELS), and density functional theory (DFT) calculations were further performed to determine the accurate chemical states of Mo and charge transfer behaviors in the catalyst. As shown in Figure 2a, Mo 3d XPS spectra of GDY@MoO$_x$ can be deconvoluted into two sets of peaks, which correspond to Mo^{5+} d$_{5/2}$/d$_{3/2}$ (231.87 and 235.07 eV) and Mo^{6+} d$_{5/2}$/d$_{3/2}$ (232.38 and 235.57 eV), respectively.[62,63] For pure MoO$_3$, the valence state of Mo species is demonstrated to be +6. These results reveal the obvious charge transfer from GDY to Mo and the formation of the mixed valent states of Mo^{5+}/Mo^{6+} (ratio of Mo^{5+}/Mo^{6+} is 0.54) in GDY@MoO$_x$. Compared with pure GDY, the C 1s XPS spectra of GDY@MoO$_x$ show two additional peaks for Mo−C (283.6 eV) and the $\pi−\pi^*$ transition (288.87 eV) (Figure 2b and Table S1). The positive and negative shifts in binding energies for C 1s and Mo 3d in GDY@MoO$_x$, respectively, reveal that the electrons transfer from GDY to MoO$_x$ QDs. Moreover, the O 1s (Figure S6) and C 1s XPS spectra confirm the formation of C−O bonds between GDY and MoO$_x$ QDs. These results demonstrate the successful construction of a novel structure on the interface between the MoO$_x$ and the GDY with sp-C−Mo/O bonds and mixed Mo valence states. This is beneficial for enhancing the catalytic performances. The EELS results further verify the existence of Mo,[64] and one strong peak around 289 eV originates from the
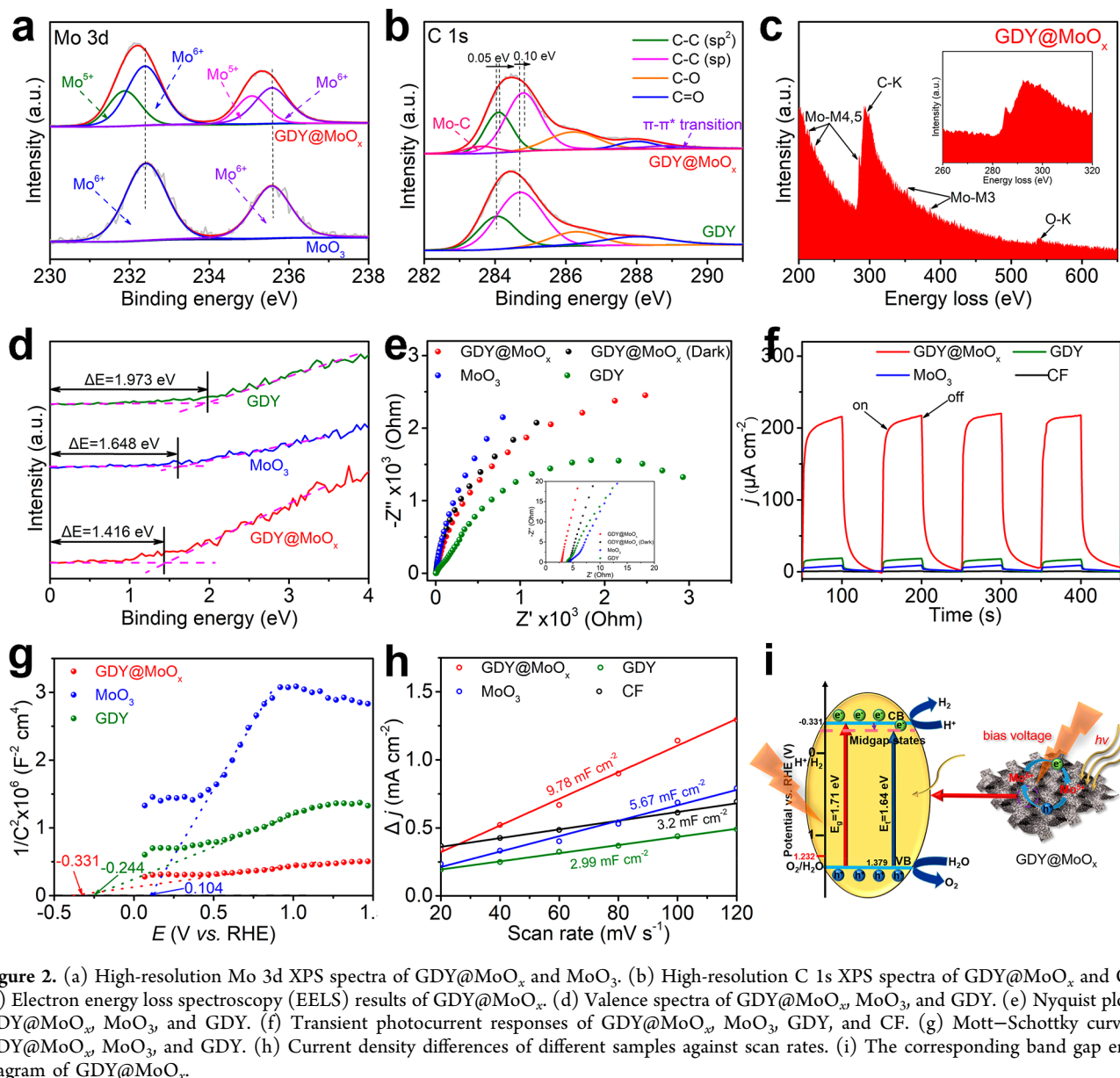
Figure 2. (a) High-resolution Mo 3d XPS spectra of GDY@MoO$_x$ and MoO$_3$. (b) High-resolution C 1s XPS spectra of GDY@MoO$_x$ and GDY. (c) Electron energy loss spectroscopy (EELS) results of GDY@MoO$_x$. (d) Valence spectra of GDY@MoO$_x$, MoO$_3$, and GDY. (e) Nyquist plots of GDY@MoO$_x$, MoO$_3$, and GDY. (f) Transient photocurrent responses of GDY@MoO$_x$, MoO$_3$, GDY, and CF. (g) Mott−Schottky curves of GDY@MoO$_x$, MoO$_3$, and GDY. (h) Current density differences of different samples against scan rates. (i) The corresponding band gap energy diagram of GDY@MoO$_x$.

interplays of Mo and C (Figures 2c and S7). The top of the valence band of GDY@MoO$_x$ (ΔE = 1.416 eV) is closer to the Fermi level than those of GDY (ΔE = 1.904 eV) and MoO$_3$ (ΔE = 1.648 eV) (Figure 2d), which indicates the improved conductivity of the catalyst. The formation energies for C−Mo/C−O interfacial chemical bonds were calculated theoretically. It is found that the formation energy for (C−Mo)/(C−O) bonds (−3.33 eV) at the interfacial structures of GDY@MoO$_x$ is much lower than that of C−O bonds. This reveals the higher stability of (C−Mo)/(C−O) bonds than C−O bonds. Bader charge analysis indicates that the charge transfer between GDY and MoO$_x$ QDs is multiplied for the catalyst with two bonding types (Figure S8). Combined with the electron donor property of GDY revealed by XPS, we can speculate it is the (C−Mo)/(C−O) bonds that play a bridge role in transferring electrons, which would produce more active sites, facilitate charge transfer, and thus result in higher intrinsic activity. These results reveal that the GDY plays an important role in the controllable synthesis of QDs. The light absorption properties of GDY@MoO$_x$, MoO$_3$, and GDY were

determined over the wavelength range of 400−800 nm. As shown in Figure S9, GDY@MoO$_x$ has an obvious UV absorption peak at 520 nm. The band gaps (E_g) of GDY@MoO$_x$, MoO$_3$, and GDY are calculated to be 1.71, 2.89, and 2.21 eV, respectively, according to the transformed Kubelka−Munk function (Figure S10).[65] The smallest band gap of GDY@MoO$_x$ broadens its optical absorption range and thus improves the light utilization. Besides, GDY@MoO$_x$ has a smaller transition energy (E_t) from VB to the midgap state than MoO$_3$ and GDY, which indicates the GDY@MoO$_x$ would be easier to generate free electrons and holes and improve the conductivity (Figure 2i). In the experiments, an external positive bias is applied to drive these photogenerated electron−hole pairs in opposite directions to delay their recombination rates, which can therefore significantly enhance the catalytic activity. Besides, GDY@MoO$_x$ has a smaller ionization energy (IE) of 5.71 eV, suggesting that GDY@MoO$_x$ is more propitious to photoelectrocatalysis (Figure S11). As shown in Figure 2g, GDY@MoO$_x$ is an n-type
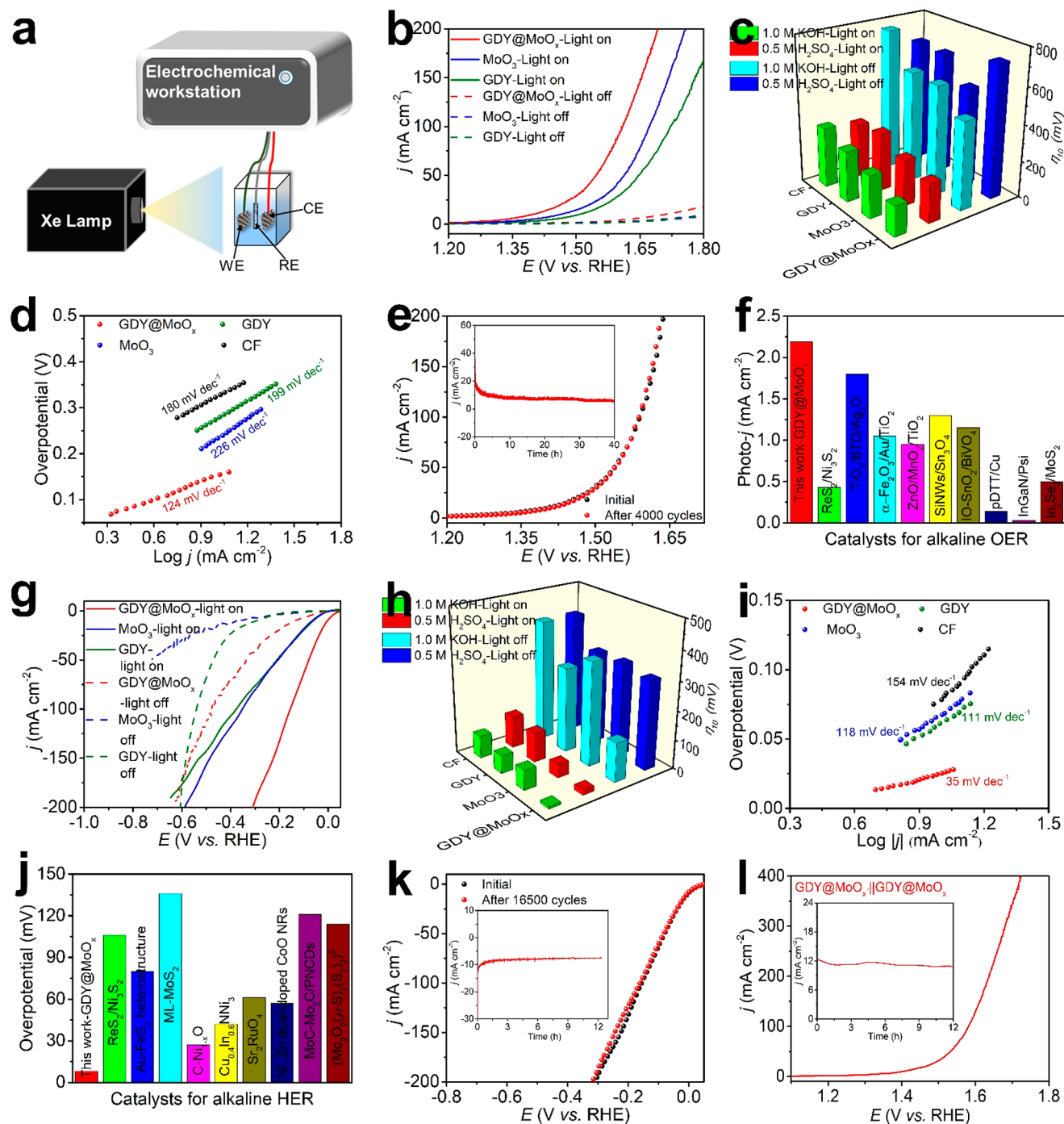
Figure 3. (a) Schematics of the PEC test. LSV (b) OER and (g) HER curves of GDY@MoO$_x$, MoO$_3$, and GDY in 1.0 M KOH. Overpotentials of (c) OER and (h) HER of GDY@MoO$_x$, MoO$_3$, GDY, and CF under different conditions: light on in 0.5 M H$_2$SO$_4$ (red column), light off in 0.5 M H$_2$SO$_4$ (blue column), light on in 1.0 M KOH (green column), light off in 1.0 M KOH (cyan column). In 1.0 M KOH: Tafel plots of (d) OER and (i) HER performance of GDY@MoO$_x$, MoO$_3$, GDY, and CF. (e) Polarization curves of OER of GDY@MoO$_x$ before and after 4000 CV cycles (inset: the time-dependent current density curve). (f) Comparison of the photocurrent density at 1.23 V (vs. RHE) of GDY@MoO$_x$ recorded at 10 mA cm^{-2} with reported alkaline OER catalysts. (j) Comparison of the overpotential of GDY@MoO$_x$ recorded at 10 mA cm^{-2} with reported alkaline HER catalysts. (k) Polarization curves of HER of GDY@MoO$_x$ before and after 16 500 CV cycles (inset: the time-dependent current density curve). (l) PEC overall water splitting performances of GDY@MoO$_x$ (inset: the time-dependent current density curve).

catalyst with a more negative E_{fb}, which satisfies the thermodynamic requirements for the water reduction.

Figure 2e shows the Nyquist plots of the samples fitted by an R(QR)(QR) equivalent circuit model comprising solution resistance (R_s), charge transfer resistance (R_{ct}), and adsorption resistance (R'). As illustrated in Table S2, GDY@MoO$_x$ under

irradiation exhibits R_s and R_{ct} values of 2.9 and 2.8 Ω, which are smaller than those of GDY@MoO$_x$ without irradiation (4.1 and 9296 Ω) (Figures S12 and S13), MoO$_3$ (4.6 and 4046 Ω) and GDY (4.0 and 3539 Ω), respectively. This indicates the fastest charge transfer behavior, lowest adsorption resistance, and highest conductivity of GDY@MoO$_x$ under irradiation for

PEC reactions. Besides, the double-layered capacitance (C_{dl}) of the catalysts was determined via the cyclic voltammetry method (Figure S14) in the non-Faradaic range (0.05−0.15 V vs. SCE) to obtain their electrochemical surface area (ECSA). As shown in Figure 2h, GDY@MoO$_x$ shows the largest C_{dl} value of 9.78 mF cm^{-2}, which is about 1.72 times greater than bulk MoO$_3$ (5.67 mF cm^{-2}), 3.27 times greater than GDY (2.99 mF cm^{-2}), and 3.06 times greater than CF (3.2 mF cm^{-2}). The ECSA for GDY@MoO$_x$ was calculated to be 244.5 cm^2 according to previous reports.[66] When the repeated on−off cycles of white-light irradiation are applied, quick, stable, and reproducible photocurrents appear (Figure 2f). GDY@MoO$_x$ can reach a larger photocurrent of 220.1 μA cm^{-2}, which is 24.5, 11.6, and 244.6 times higher than that of MoO$_3$ (9.0 μA cm^{-2}), GDY (19.0 μA cm^{-2}), and CF (0.9 μA cm^{-2}), respectively. The nearly vertical variation of current suggests the fast charge transfer in GDY@MoO$_x$, while the slowly accumulating charge transfer process indicates that the introduction of GDY can effectively inhibit the charge recombination. These advantages of GDY@MoO$_x$ are beneficial for generating more active sites, improving the conductivity, and finally enhancing the catalytic activity.

## 3.2. Photoelectrocatalytic Performances of GDY@MoO$_x$

The PEC performances of the samples for HER, OER, and OWS were studied using a typical three-electrode system (Figure 3a). Figure 3b shows the polarization curves of the samples obtained with or without irradiation in 1.0 M KOH. Obviously, GDY@MoO$_x$ exhibits the smallest overpotential of 165 mV at the current density (j) of 10 mA cm^{-2} under the irradiation of the xenon lamp, which is better than the GDY@MoO$_x$ without irradiation (478 mV@10 mA cm^{-2}), MoO$_3$ (231 mV@10 mA cm^{-2}), GDY (275 mV@10 mA cm^{-2}), and CF (325 mV@10 mA cm^{-2}), respectively (Figure 3c). The PEC OER kinetics was studied from Tafel analysis based on the overpotential versus the logarithm of current density. As expected, GDY@MoO$_x$ shows the smallest Tafel slope of 124 mV dec^{-1} compared to those of MoO$_3$ (226 mV dec^{-1}), GDY (199 mV dec^{-1}), and CF (180 mV dec^{-1}) (Figure 3d). Besides, the long-term stability of the catalyst was tested and is shown in Figure 3e. There is a slight decrease in the current density after 4000 CV cycling tests, as compared to the as-prepared catalyst. Such an excellent OER activity of GDY@MoO$_x$ can also be well-maintained at 10 mA cm^{-2} for 40 h (Figures S15 and S16). In addition, GDY@MoO$_x$ shows a much higher photocurrent density at 1.23 V (vs. RHE) than reported catalysts (Figure 3f and Table S3), verifying the generation of photoinduced charges. Remarkably, GDY@MoO$_x$ also exhibits excellent OER performance in acidic conditions with the smallest overpotential of 214 mV at 10 mA cm^{-2} and a Tafel slope of 152 mV dec^{-1} (Figures S17). These values are better than reported ones.[60,67,68]

The PEC HER activity of GDY@MoO$_x$ was next studied in alkaline conditions (Figure 3g). As expected, GDY@MoO$_x$ exhibits the best HER activity with the smallest overpotential of 8 mV at 10 mA cm^{-2} and the smallest Tafel slope of 35 mV dec^{-1} under illumination compared to that of the dark condition (135 mV@10 mA cm^{-2}, 229 mV dec^{-1}), MoO$_3$ (69 mV@10 mA cm^{-2}, 118 mV dec^{-1}), GDY (62 mV@10 mA cm^{-2}, 111 mV dec^{-1}) (Figure 3h,i), and other reported benchmarked catalysts (Figure 3j). The catalyst also exhibits high catalytic stability with a negligible decrease in current density after the 16 500 CV cycling cycles (Figure 3k). The

HER performance of GDY@MoO$_x$ under acidic conditions was also studied and provided in the SI (Figures S18 and S19). In view of the outstanding OER and HER performances, GDY@MoO$_x$ was directly used as the anode and cathode for OWS measurements in 1.0 M KOH and 0.5 M H$_2$SO$_4$ (Figures 3l and S20). Remarkably, the GDY@MoO$_x$||GDY@MoO$_x$ system requires a very small cell voltage of 1.40 V to deliver 10 mA cm^{-2}, which can be maintained over 12 h for continuous electrolysis.

3.3. Theoretical Study

DFT calculations were further performed to study the activity origin of GDY@MoO$_x$ toward highly efficient overall water splitting. According to the total density of states (TDOS), bulk MoO$_3$ is a semiconductor with a large band gap and poor conductivity, while the band gap of GDY@MoO$_x$ is significantly reduced mainly because the position of conduction band minimum (CBM) obviously moves down, thereby enhancing the conductivity (Figure 4a). In addition,
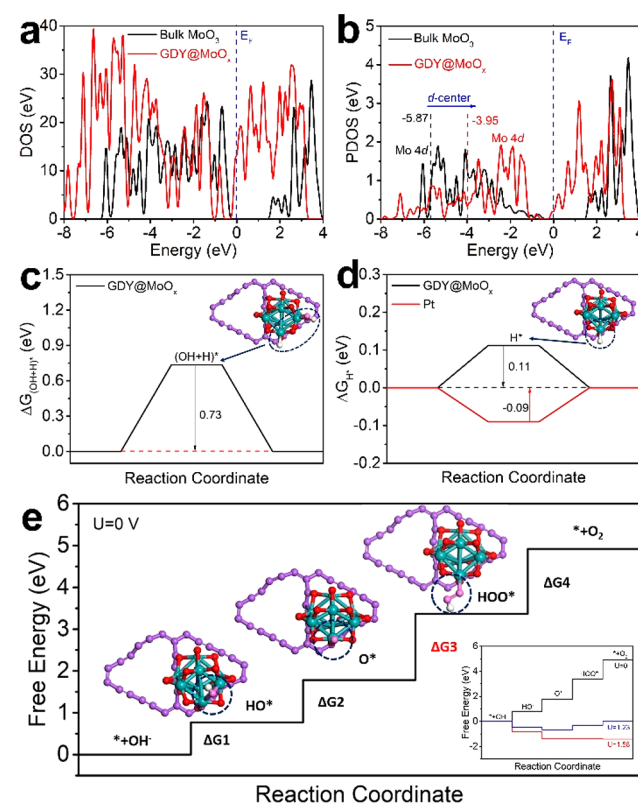
Figure 4. (a) TDOS and (b) PDOS of bulk MoO$_3$ and GDY@MoO$_x$. (c,d) Water activation and hydrogen evolution reaction process. (e) Water oxidation and oxygen evolution reaction process.

according to the projected density of states (PDOS) of the Mo site, the d-band of the Mo atom in GDY@MoO$_x$ obviously shifts to the right, much closer to the Fermi level (Figure 4b). This indicates that GDY can effectively donate electrons to the Mo site and upshift the d-band center position of metallic Mo from −5.87 eV (bulk MoO$_3$) to −3.95 eV (MoO$_x$ QDs). The d-center upshift of the Mo site leads to the catalytic activity enhancement of GDY@MoO$_x$. It is shown that the decomposition of a water molecule (the starting step of the whole reaction) only requires a low Gibbs free energy ($\Delta G_{(OH+H)*}$) of 0.73 eV (Figure 4c). The free energy for HER is calculated to be 0.11 eV (ΔG_{H*}), close to pure Pt

(∼−0.09 eV) (Figure 4d), revealing the high HER activity of the Mo sites in the catalyst. The OER is a four-electron process, which can spontaneously proceed under an external potential of 1.58 V (Figure 4e). Among the four steps, the oxidation of intermediate O* to form HOO* is the determining step of OER with a ΔG_3 of 1.58 eV, close to the ideal ΔG of 1.23 eV. We can evaluate the OER activity of GDY@MoO_x catalyst using the potential (η), which is calculated as $\eta = [\max(\Delta G1, \Delta G2, \Delta G1, \Delta G2) - 1.23]/e = 0.35$ V, much lower than the previously reported ones.[69−71] These all verify the excellent oxygen evolution activity of GDY@MoO_x.

4. CONCLUSIONS

By using GDY as the ideal platform, we have proposed a facile synthetic strategy for the successful fabrication of GDY@MoO_x heterojunctions for PEC water splitting. Experimental and DFT calculation results reveal the construction of a novel structure on the interface, containing sp-C−Mo/O bonds and mixed Mo valence states, show outstanding catalytic activity and stability for photoelectrocatalytic overall water splitting in a wide pH range (0−14), due to the presence of sp-carbon-rich GDY. The reaction mechanisms were well-studied, revealing that the *d*-center upshift of the Mo site leads to the catalytic activity enhancement of GDY@MoO_x. In addition, GDY@MoO_x performs well in extreme environments, only needing 1.40 or 1.39 V of the cell voltage to deliver 10 mA cm^{-2} with tolerable stability under alkaline or acidic conditions. This work demonstrates clearly the important role of graphdiyne in the controllable fabrication of high-performance PEC catalysts with accurate interfacial structures and valence states.

ASSOCIATED CONTENT

Ⓢ Supporting Information

The Supporting Information is available free of charge at https://pubs.acs.org/doi/10.1021/acsmaterialsau.1c00071.

> Characterizations, photoelectrochemical studies, computational details, supplementary figures, and supplementary tables (PDF)

AUTHOR INFORMATION

Corresponding Authors

Yurui Xue − *Institute of Chemistry, Chinese Academy of Sciences, Beijing 100190, P.R. China; Science Center for Material Creation and Energy Conversion, Institute of Frontier and Interdisciplinary Science, School of Chemistry and Chemical Engineering, Shandong University, Jinan 250100, P.R. China*; Email: yrxue@sdu.edu.cn

Yuliang Li − *Institute of Chemistry, Chinese Academy of Sciences, Beijing 100190, P.R. China; University of Chinese Academy of Sciences, Beijing 100049, P.R. China;* ⬤ orcid.org/0000-0001-5279-0399; Email: ylli@iccas.ac.cn

Authors

Xi Chen − *Institute of Chemistry, Chinese Academy of Sciences, Beijing 100190, P.R. China; University of Chinese Academy of Sciences, Beijing 100049, P.R. China*

Xuchen Zheng − *Institute of Chemistry, Chinese Academy of Sciences, Beijing 100190, P.R. China; University of Chinese Academy of Sciences, Beijing 100049, P.R. China*

Lu Qi − *Science Center for Material Creation and Energy Conversion, Institute of Frontier and Interdisciplinary Science, School of Chemistry and Chemical Engineering, Shandong University, Jinan 250100, P.R. China*

Complete contact information is available at:
https://pubs.acs.org/10.1021/acsmaterialsau.1c00071

Author Contributions

Y.L. conceived and designed the research and critically revised the manuscript. X.C. synthesized the catalysts and carried out the experiments. X.Z. and L.Q. gave useful help during the synthesis and morphological characterization processes. Y.X. assisted the data analysis and organized and wrote the draft.

Notes

The authors declare no competing financial interest.

■ ACKNOWLEDGMENTS

■ REFERENCES

(1) Cook, T. R.; Dogutan, D. K.; Reece, S. Y.; Surendranath, Y.; Teets, T. S.; Nocera, D. G. Solar energy supply and storage for the legacy and nonlegacy worlds. *Chem. Rev.* **2010**, *110* (11), 6474−6502.

(2) Stolley, R. M.; Helm, M. L. Light-harvesting materials: soft support for energy conversion. *Nat. Chem.* **2014**, *6* (11), 949−950.

(3) Roger, I.; Shipman, M. A.; Symes, M. D. Earth-abundant catalysts for electrochemical and photoelectrochemical water splitting. *Nat. Rev. Chem.* **2017**, *1* (1), 0003.

(4) Liyanage, D. R.; Li, D.; Cheek, Q. B.; Baydoun, H.; Brock, S. L. Synthesis and oxygen evolution reaction (OER) catalytic performance of $Ni_{2-x}Ru_xP$ nanocrystals: enhancing activity by dilution of the noble metal. *J. Mater. Chem. A* **2017**, *5* (33), 17609−17618.

(5) Zhang, N.; Qi, M.; Yuan, L.; Fu, X.; Tang, Z.; Gong, J.; Xu, Y. Broadband light harvesting and unidirectional electron flow for efficient electron accumulation for hydrogen generation. *Angew. Chem.* **2019**, *131* (29), 10108−10112.

(6) Balog, Á.; Samu, G. F.; Pető, S.; Janáky, C. The mystery of black TiO_2: insights from combined surface science and in situ electrochemical methods. *ACS Mater. Au* **2021**, *1* (2), 157−168.

(7) Zhang, H.; Zhang, P.; Qiu, M.; Dong, J.; Zhang, Y.; Lou, X. W. D. Ultrasmall MoO_x clusters as a novel cocatalyst for photocatalytic hydrogen evolution. *Adv. Mater.* **2019**, *31* (6), 1804883.

(8) Yu, H.; Liu, Y.; Brock, S. L. Tuning the optical band gap of quantum dot assemblies by varying network density. *ACS Nano* **2009**, *3* (7), 2000−2006.

(9) Li, M.; Xia, Z. Recent progress of zero-dimensional luminescent metal halides. *Chem. Soc. Rev.* **2021**, *50* (4), 2626−2662.

(10) Liu, Y.; Nag, A.; Manna, L.; Xia, Z. Lead-free double perovskite $Cs_2AgInCl_6$. *Angew. Chem., Int. Ed.* **2021**, *60* (21), 11592−11603.

(11) Cai, R.; Milton, R. D.; Abdellaoui, S.; Park, T.; Patel, J.; Alkotaini, B.; Minteer, S. D. Electroenzymatic C-C bond formation from CO_2. *J. Am. Chem. Soc.* **2018**, *140* (15), 5041−5044.

(12) Kankala, R. K.; Zhang, H.; Liu, C. G.; Kanubaddi, K. R.; Lee, C. H.; Wang, S. B.; Cui, W.; Santos, H. A.; Lin, K.; Chen, A. Z. Metal species−encapsulated mesoporous silica nanoparticles: current advancements and latest breakthroughs. *Adv. Funct. Mater.* **2019**, *29* (43), 1902652.

(13) Chen, H.; Prater, M. B.; Cai, R.; Dong, F.; Chen, H.; Minteer, S. D. Bioelectrocatalytic conversion from N_2 to chiral amino acids in a H_2/α-Keto acid enzymatic fuel cell. *J. Am. Chem. Soc.* **2020**, *142* (8), 4028−4036.

(14) Kankala, R. K.; Han, Y. H.; Na, J.; Lee, C. H.; Sun, Z.; Wang, S. B.; Kimura, T.; Ok, Y. S.; Yamauchi, Y.; Chen, A. Z.; Wu, K. C. Nanoarchitectured structure and surface biofunctionality of mesoporous silica nanoparticles. *Adv. Mater.* **2020**, *32* (23), 1907035.

(15) Shamsi, J.; Rainò, G.; Kovalenko, M. V.; Stranks, S. D. To nano or not to nano for bright halide perovskite emitters. *Nat. Nanotechnol.* **2021**, *16*, 1164−1168.

(16) Montanarella, F.; McCall, K. M.; Sakhatskyi, K.; Yakunin, S.; Trtik, P.; Bernasconi, C.; Cherniukh, I.; Mannes, D.; Bodnarchuk, M. I.; Strobl, M.; Walfort, B.; Kovalenko, M. V. Highly concentrated, zwitterionic ligand-capped Mn^{2+}: $CsPb(Br_xCl_{1-x})_3$ nanocrystals as bright scintillators for fast neutron imaging. *ACS Energy Lett.* **2021**, *6*, 4365−4373.

(17) Kim, J.; Choi, S.; Cho, J.; Kim, S. Y.; Jang, H. W. Toward multicomponent single-atom catalysis for efficient electrochemical energy conversion. *ACS Mater. Au* **2021**, *2*, 1.

(18) Seh, Z. W.; Kibsgaard, J.; Dickens, C. F.; Chorkendorff, I.; Nørskov, J. K.; Jaramillo, T. F. Combining theory and experiment in electrocatalysis: insights into materials design. *Science* **2017**, *355*, No. eaad4998.

(19) Lu, K. Q.; Li, Y. H.; Zhang, F.; Qi, M. Y.; Chen, X.; Tang, Z. R.; Yamada, Y. M. A.; Anpo, M.; Conte, M.; Xu, Y. J. Rationally designed transition metal hydroxide nanosheet arrays on graphene for artificial CO_2 reduction. *Nat. Commun.* **2020**, *11* (1), 5181.

(20) Li, G.; Li, Y.; Liu, H.; Guo, Y.; Li, Y.; Zhu, D. Architecture of graphdiyne nanoscale films. *Chem. Commun. (Camb)* **2010**, *46* (19), 3256−3258.

(21) Huang, C.; Li, Y.; Wang, N.; Xue, Y.; Zuo, Z.; Liu, H.; Li, Y. Progress in research into 2d graphdiyne-based materials. *Chem. Rev.* **2018**, *118* (16), 7744−7803.

(22) Zuo, Z.; Li, Y. Emerging electrochemical energy applications of graphdiyne. *Joule* **2019**, *3* (4), 899−903.

(23) Sakamoto, R.; Fukui, N.; Maeda, H.; Matsuoka, R.; Toyoda, R.; Nishihara, H. The accelerating world of graphdiynes. *Adv. Mater.* **2019**, *31* (42), 1804211.

(24) Liu, J.; Chen, C.; Zhao, Y. Progress and prospects of graphdiyne-based materials in biomedical applications. *Adv. Mater.* **2019**, *31* (42), 1804386.

(25) Du, Y.; Zhou, W.; Gao, J.; Pan, X.; Li, Y. Fundament and application of graphdiyne in electrochemical energy. *Acc. Chem. Res.* **2020**, *53* (2), 459−469.

(26) Li, J.; Gao, X.; Zhu, L.; Ghazzal, M. N.; Zhang, J.; Tung, C.-H.; Wu, L. Graphdiyne for crucial gas involved catalytic reactions in energy conversion applications. *Energy Environ. Sci.* **2020**, *13* (5), 1326−1346.

(27) Zhan, S.; Zhao, Y.; Yang, N.; Wang, D. Pore structure of graphdiyne design: synthesis and application. *Chem. J. Chinese U.* **2021**, *42* (2), 333−348.

(28) Zhang, H.; Wang, Y.; Liu, P.; Han, Y.; Yao, X.; Zou, J.; Cheng, H.; Zhao, H. Anatase TiO_2 crystal facet growth: mechanistic role of hydrofluoric acid and photoelectrocatalytic activity. *ACS Appl. Mater. Interfaces* **2011**, *3* (7), 2472−2478.

(29) Yang, N.; Liu, Y.; Wen, H.; Tang, Z.; Zhao, H.; Li, Y.; Wang, D. Photocatalytic properties ofgraphdiyne and graphene modifiedTiO₂: from theory to experiment. *ACS Nano* **2013**, *7* (2), 1504−1512.

(30) Li, J.; Gao, X.; Liu, B.; Feng, Q. L.; Li, X. B.; Huang, M. Y.; Liu, Z. F.; Zhang, J.; Tung, C. H.; Wu, L. Z. Graphdiyne: a metal-free material as hole transfer layer to fabricate quantum dot-sensitized photocathodes for hydrogen production. *J. Am. Chem. Soc.* **2016**, *138* (12), 3954−3957.

(31) Gao, X.; Zhou, J.; Du, R.; Xie, Z.; Deng, S.; Liu, R.; Liu, Z.; Zhang, J. Robust superhydrophobic foam: a graphdiyne-based hierarchical architecture for oil/water separation. *Adv. Mater.* **2016**, *28* (1), 168−173.

(32) Parvin, N.; Jin, Q.; Wei, Y.; Yu, R.; Zheng, B.; Huang, L.; Zhang, Y.; Wang, L.; Zhang, H.; Gao, M.; Zhao, H.; Hu, W.; Li, Y.; Wang, D. Few-layer graphdiyne nanosheets applied for multiplexed real-time DNA detection. *Adv. Mater.* **2017**, *29* (18), 1606755.

(33) Yu, H.; Xue, Y.; Hui, L.; Zhang, C.; Li, Y.; Zuo, Z.; Zhao, Y.; Li, Z.; Li, Y. Efficient Hydrogen Production on a 3D Flexible Heterojunction Material. *Adv. Mater.* **2018**, *30* (21), 1707082.

(34) Li, C.; Lu, X.; Han, Y.; Tang, S.; Ding, Y.; Liu, R.; Bao, H.; Li, Y.; Luo, J.; Lu, T. Direct imaging and determination of the crystal structure of six-layered graphdiyne. *Nano Res.* **2018**, *11* (3), 1714−1721.

(35) Yang, P.; Zou, X.; Zhang, Z.; Hong, M.; Shi, J.; Chen, S.; Shu, J.; Zhao, L.; Jiang, S.; Zhou, X.; Huan, Y.; Xie, C.; Gao, P.; Chen, Q.; Zhang, Q.; Liu, Z.; Zhang, Y. Batch production of 6-in. uniform monolayer molybdenum disulfide catalyzed by sodium in glass. *Nat. Commun.* **2018**, *9* (1), 979.

(36) Zhao, Y.; Wan, J.; Yao, H.; Zhang, L.; Lin, K.; Wang, L.; Yang, N.; Liu, D.; Song, L.; Zhu, J.; Gu, L.; Liu, L.; Zhao, H.; Li, Y.; Wang, D. Few-layer graphdiyne doped with sp-hybridized nitrogen atoms at acetylenic sites for oxygen reduction electrocatalysis. *Nat. Chem.* **2018**, *10* (9), 924−931.

(37) Xue, Y.; Hui, L.; Yu, H.; Liu, Y.; Fang, Y.; Huang, B.; Zhao, Y.; Li, Z.; Li, Y. Rationally engineered active sites for efficient and durable hydrogen generation. *Nat. Commun.* **2019**, *10* (1), 2281.

(38) Gao, X.; Liu, H.; Wang, D.; Zhang, J. Graphdiyne: synthesis, properties, and applications. *Chem. Soc. Rev.* **2019**, *48* (3), 908−936.

(39) Zhao, Y.; Yang, N.; Yao, H.; Liu, D.; Song, L.; Zhu, J.; Li, S.; Gu, L.; Lin, K.; Wang, D. Stereodefined codoping of sp-N and S atoms in few-layer graphdiyne for oxygen evolution reaction. *J. Am. Chem. Soc.* **2019**, *141* (18), 7240−7244.

(40) Huang, L.; Chen, D.; Luo, G.; Lu, Y. R.; Chen, C.; Zou, Y.; Dong, C. L.; Li, Y.; Wang, S. Zirconium-regulation-induced bifunctionality in 3D cobalt-iron oxide nanosheets for overall water splitting. *Adv. Mater.* **2019**, *31* (28), 1901439.

(41) Zheng, J.; Lyu, Y.; Qiao, M.; Wang, R.; Zhou, Y.; Li, H.; Chen, C.; Li, Y.; Zhou, H.; Jiang, S. P.; Wang, S. Photoelectrochemical synthesis of ammonia on the aerophilic-hydrophilic heterostructure with 37.8% efficiency. *Chem.* **2019**, *5* (3), 617−633.

(42) Fang, Y.; Xue, Y.; Li, Y.; Yu, H.; Hui, L.; Liu, Y.; Xing, C.; Zhang, C.; Zhang, D.; Wang, Z.; Chen, X.; Gao, Y.; Huang, B.; Li, Y. Graphdiyne interface engineering: highly active and selective ammonia synthesis. *Angew. Chem., Int. Ed.* **2020**, *59* (31), 13021−13027.

(43) Zhang, S.; Si, H.; Fan, W.; Shi, M.; Li, M.; Xu, C.; Zhang, Z.; Liao, Q.; Sattar, A.; Kang, Z.; Zhang, Y. Graphdiyne: bridging SnO_2 and perovskite in planar solar cells. *Angew. Chem., Int. Ed.* **2020**, *59* (28), 11573−11582.

(44) Jia, Y.; Yao, X. Heteroatom-doped graphdiyne enables ferromagnetism of carbon. *ACS Cent. Sci.* **2020**, *6* (6), 830−832.

(45) Liu, Y.; Xue, Y.; Yu, H.; Hui, L.; Huang, B.; Li, Y. Graphdiyne ultrathin nanosheets for efficient water splitting. *Adv. Funct. Mater.* **2021**, *31* (16), 2010112.

(46) Fang, Y.; Xue, Y.; Hui, L.; Yu, H.; Li, Y. Graphdiyne@Janus magnetite for photocatalytic nitrogen fixation. *Angew. Chem., Int. Ed.* **2021**, *60* (6), 3170−3174.

(47) Yao, Y.; Zhu, Y.; Pan, C.; Wang, C.; Hu, S.; Xiao, W.; Chi, X.; Fang, Y.; Yang, J.; Deng, H.; Xiao, S.; Li, J.; Luo, Z.; Guo, Y. Interfacial sp C-O-Mo hybridization originated high-current density hydrogen evolution. *J. Am. Chem. Soc.* **2021**, *143* (23), 8720−8730.

(48) Wen, J.; Tang, W.; Kang, Z.; Liao, Q.; Hong, M.; Du, J.; Zhang, X.; Yu, H.; Si, H.; Zhang, Z.; Zhang, Y. Direct charge trapping multilevel memory with graphdiyne/MoS₂ Van der Waals heterostructure. *Adv. Sci.* **2021**, *8* (21), 2101417.

(49) Navaee, A.; Salimi, A.; Sham, T.-K. Bipolar electrochemistry as a powerful technique for rapid synthesis of ultrathin graphdiyne nanosheets: Improvement of photoelectrocatalytic activity toward both hydrogen and oxygen evolution. *Int. J. Hydrog. Energy* **2021**, *46* (24), 12906−12914.

(50) Zheng, Z.; Wang, Z.; Xue, Y.; He, F.; Li, Y. Selective conversion of CO_2 into cyclic carbonate on atom level catalysts. *ACS Mater. Au* **2021**, *1* (2), 107−115.

(51) Ren, H.; Shao, H.; Zhang, L.; Guo, D.; Jin, Q.; Yu, R.; Wang, L.; Li, Y.; Wang, Y.; Zhao, H.; Wang, D. A new graphdiyne

nanosheet/Pt nanoparticle-basedcounter electrode material with enhanced catalytic activityfor dye-sensitized solar cells. *Adv. Energy Mater.* **2015**, *5* (12), 1500296.

(52) Li, J.; Gao, X.; Liu, B.; Feng, Q.; Li, X. B.; Huang, M. Y.; Liu, Z.; Zhang, J.; Tung, C. H.; Wu, L. Z. Graphdiyne: a metal-free material as hole transfer layer to fabricate quantum dot-sensitized photocathodes for hydrogen production. *J. Am. Chem. Soc.* **2016**, *138* (12), 3954−3957.

(53) Zhao, Y.; Tang, H.; Yang, N.; Wang, D. Graphdiyne: recent achievements in photo- andelectrochemical conversion. *Adv. Sci.* **2018**, *5* (12), 1800959.

(54) Du, Y.; Xue, Y.; Zhang, C.; Liu, Y.; Fang, Y.; Xing, C.; He, F.; Li, Y. Photoinduced electrocatalysis on 3D flexible OsO$_x$ quantum dots. *Adv. Energy Mater.* **2021**, *11* (18), 2100234.

(55) Matsuoka, R.; Sakamoto, R.; Hoshiko, K.; Sasaki, S.; Masunaga, H.; Nagashio, K.; Nishihara, H. Crystalline graphdiyne nanosheets produced at a gas/liquid orliquid/liquid interface. *J. Am. Chem. Soc.* **2017**, *139*, 3145−3152.

(56) Gao, X.; Li, J.; Du, R.; Zhou, J.; Huang, M.; Liu, R.; Li, J.; Xie, Z.; Wu, L.; Liu, Z.; Zhang, J. Direct synthesis of graphdiyne nanowalls on arbitrarysubstrates and its application for photoelectrochemical-water splitting cell. *Adv. Mater.* **2017**, *29* (9), 1605308.

(57) Xue, Y.; Huang, B.; Yi, Y.; Guo, Y.; Zuo, Z.; Li, Y.; Jia, Z.; Liu, H.; Li, Y. Anchoring zero valence single atoms of nickel and iron on graphdiyne for hydrogen evolution. *Nat. Commun.* **2018**, *9*, 1460.

(58) Hui, L.; Xue, Y.; Yu, H.; Liu, Y.; Fang, Y.; Xing, C.; Huang, B.; Li, Y. Highly efficient and selective generation of ammonia and hydrogen on a graphdiyne-based catalyst. *J. Am. Chem. Soc.* **2019**, *141* (27), 10677−10683.

(59) Yu, H.; Xue, Y.; Hui, L.; Zhang, C.; Fang, Y.; Liu, Y.; Chen, X.; Zhang, D.; Huang, B.; Li, Y. Graphdiyne-based metal atomic catalysts for synthesizing ammonia. *Natl. Sci. Rev.* **2021**, *8* (8), No. nwaa213.

(60) Xing, C.; Xue, Y.; Huang, B.; Yu, H.; Hui, L.; Fang, Y.; Liu, Y.; Zhao, Y.; Li, Z.; Li, Y. Fluorographdiyne: a metal-free catalyst for applications in water reduction and oxidation. *Angew. Chem., Int. Ed.* **2019**, *58* (39), 13897−13903.

(61) Camacho-López, M. A.; Escobar-Alarcón, L.; Picquart, M.; Arroyo, R.; Córdoba, G.; Haro-Poniatowski, E. Micro-Raman study of the m-MoO$_2$ to α-MoO$_3$ transformation induced by cw-laser irradiation. *Opt. Mater.* **2011**, *33* (3), 480−484.

(62) Vasilopoulou, M.; Douvas, A. M.; Georgiadou, D. G.; Palilis, L. C.; Kennou, S.; Sygellou, L.; Soultati, A.; Kostis, I.; Papadimitropoulos, G.; Davazoglou, D.; Argitis, P. The influence of hydrogenation and oxygen vacancies on molybdenum oxides work function and gap states for application in organic optoelectronics. *J. Am. Chem. Soc.* **2012**, *134* (39), 16178−16187.

(63) Men, Y. L.; You, Y.; Pan, Y. X.; Gao, H.; Xia, Y.; Cheng, D. G.; Song, J.; Cui, D. X.; Wu, N.; Li, Y.; Xin, S.; Goodenough, J. B. Selective CO evolution from photoreduction of CO$_2$ on a metal-carbide-based composite catalyst. *J. Am. Chem. Soc.* **2018**, *140* (40), 13071−13077.

(64) Shon, J. K.; Lee, H. S.; Park, G. O.; Yoon, J.; Park, E.; Park, G. S.; Kong, S. S.; Jin, M.; Choi, J. M.; Chang, H.; Doo, S.; Kim, J. M.; Yoon, W. S.; Pak, C.; Kim, H.; Stucky, G. D. Discovery of abnormal lithium-storage sites in molybdenum dioxide electrodes. *Nat. Commun.* **2016**, *7*, 11049.

(65) Ran, J.; Ma, T. Y.; Gao, G.; Du, X.-W.; Qiao, S. Z. Porous P-doped graphitic carbon nitride nanosheets for synergistically enhanced visible-light photocatalytic H$_2$ production. *Energy Environ. Sci.* **2015**, *8* (12), 3708−3717.

(66) McCrory, C. C.; Jung, S.; Peters, J. C.; Jaramillo, T. F. Benchmarking heterogeneous electrocatalysts for the oxygen evolution reaction. *J. Am. Chem. Soc.* **2013**, *135* (45), 16977−16987.

(67) Xiong, Q.; Zhang, X.; Wang, H.; Liu, G.; Wang, G.; Zhang, H.; Zhao, H. One-step synthesis of cobalt-doped MoS$_2$ nanosheets as bifunctional electrocatalysts foroverall water splitting under both acidic andalkaline conditions. *Chem. Commun.* **2018**, *54*, 3859−3862.

(68) Tariq, M.; Wu, Y.; Ma, C.; Ali, M.; Zaman, W. Q.; Abbas, Z.; Ayub, K. S.; Zhou, J.; Wang, G.; Cao, L.; Yang, J. Boosted up stability and activity of oxygen vacancyenriched RuO$_2$/MoO$_3$ mixed oxide composite foroxygen evolution reaction. *Int. J. Hydrog. Energy* **2020**, *45* (35), 17287−17298.

(69) Li, X.; Wang, H.; Cui, Z.; Li, Y.; Xin, S.; Zhou, J.; Long, Y.; Jin, C.; Goodenough, J. B. Exceptional oxygen evolution reactivities on CaCoO$_3$ and SrCoO$_3$. *Sci. Adv.* **2019**, *5*, No. eaav6262.

(70) Li, J.; Chu, D.; Dong, H.; Baker, D. R.; Jiang, R. Boosted oxygen evolution reactivity by igniting double exchange interaction in spinel oxides. *J. Am. Chem. Soc.* **2020**, *142* (1), 50−54.

(71) Borrelli, M.; Querebillo, C. J.; Pastoetter, D. L.; Wang, T.; Milani, A.; Casari, C.; Khoa Ly, H.; He, F.; Hou, Y.; Neumann, C.; Turchanin, A.; Sun, H.; Weidinger, I. M.; Feng, X. Thiophene-based conjugated acetylenic polymers with dual active sites for efficient co-catalyst-free photoelectrochemical water reduction in alkaline medium. *Angew. Chem., Int. Ed.* **2021**, *60* (34), 18876−18881.